View metadata, citation and similar papers at core.ac.uk

brought to you by CORE

provided by Explore Bristol Research

Krupa, E., Cooper, J., Pirrera, A., & Nangia, R. (2016). Improved Aerodynamic Performance Combining Control Surface Deflections and Aeroelastic Tailoring. In *2016 Applied Aerodynamics Conference: Evolution & Innovation Continues - The Next 150 years of Concepts, Design and Operations* (pp. 12). Royal Aeronautical Society.

Peer reviewed version

Link to publication record in Explore Bristol Research

PDF-document

This is the accepted author manuscript (AAM). The final published version (version of record) is available online via Royal Aeronautical Society at http://www.aerosociety.com/News/Proceedings. Please refer to any applicable terms of use of the publisher.

University of Bristol - Explore Bristol Research

General rights

This document is made available in accordance with publisher policies. Please cite only the published version using the reference above. Full terms of use are available:
http://www.bristol.ac.uk/pure/about/ebr-terms

Improved Aerodynamic Performance Combining Control Surface Deflections and Aeroelastic Tailoring

Eduardo P. Krupa[1], Jonathan E. Cooper[2], Alberto Pirrera[3] and Raj Nangia[4]
Department of Aerospace Engineering, University of Bristol, Queen's Building, University Walk, Bristol BS8 1TR, UK.

The interplay between passive and active wing shape adaptation for improved aerostructural performance is analysed in this paper. Shape adaptation is sought as a means for load redistribution, alleviation and, in turn, weight saving. Passive aeroelastic responses are obtained by designing bend-twist coupling into a hybrid wing-box with composite skins. Active shape variations are realised via trailing edge control surfaces (similar to ailerons), distributed along the full wingspan. A bi-level design framework, incorporating gradient-based and particle swarm optimisations, is utilised to search the wing's design space for beneficial aerostructural properties and control surface deflection scheduling. Optimisation design variables include structural dimensions, composite lamination parameters, stringer position, rib orientation and spacing, and the deflections of individual control surfaces. Design constraints consist of allowable stresses and deformations, structural stability (i.e. buckling) and composites manufacturing guidelines. The design approach is shown to produce weight reductions and improved aerodynamic performance.

Keywords: aeroelastic tailoring, load alleviation, composite optimisation, active trailing edge devices.

1. Introduction

Aeroelastic tailoring is the branch of aircraft design that considers the interactions between aerodynamic loads and deformable airframes. It involves fine-tuning of wing mass distribution and stiffness properties, so that aerostructural design metrics are met, to achieve a desired performance. A more general definition is found in Shirk *et al.* [1] that describe aeroelastic tailoring as: *"the embodiment of directional stiffness into an aircraft structural design to control aeroelastic deformation, static or dynamic, in such a fashion as to affect the aerodynamic and structural performance of that aircraft in a beneficial way".*

Composite materials offer significant tailoring capabilities, because one can design a structure and its constituent material concurrently. Composites are therefore increasingly common in aerospace structures (e.g. 787 and A350).

Although passive aeroelastic tailoring has been possible since the 1980s, using both metallic and composite materials, it is expected that greater improvements in aircraft performance may be achieved via servo-aeroelastic tailoring. A discipline that aims to exploit the synergies between passive aeroelastic structural adaptation and active control of aerodynamic surfaces. The expected outcome is the creation of designs that outperform those conceived by following solely passive aeroelastic tailoring paradigms. Potential benefits include: load alleviation and management, airframe lightweighting, drag reduction, extended range and augmented control capabilities and authority.

A number of recent studies has explored either passive or active aeroelastic adaptations as a means to minimise wing weight under a variety of design constraints [2–8]. The use of active devices to control spanwise lift distribution on a composite wing structure is explored in [9], with drag reduction over a range of flight speeds as the main objective. The study demonstrates that, by combining passive stiffness tailoring with small control variations, induced drag can be reduced. For further relevant literature, the reader is referred to [10–14], that show improvements in aerodynamic performance adopting trailing edge devices, and to [15,16] that demonstrate the applicability of passive/active tailoring using anisotropic piezoelectric actuators for roll control and flutter suppression.

As regards design optimisation studies, [17,18] address the static aeroelasticity and flutter suppression for the metallic wingbox of NASA's Common Research model [19]. These optimisations consider detailed thickness variations of ribs, spars and skin patches along the wing's semispan and show that a significant mass reduction is achievable for a given flutter margin.

Despite the growing interest in passive-adaptive and active servo-aeroelastic concepts, most of the work undertaken by the technical community has focused on metallic airframes and on the optimisation of their drag and weight. In this paper, a hybrid metal-composite wingbox is tailored for load alleviation and mass saving via passive and active shape adaptation. In particular, we present a bi-level optimisation framework for the servo-aeroelastic tailoring of composite wing structures with distributed trailing edge ailerons. A total of 20 trailing edge aerodynamic control surfaces are incorporated along the wingspan in the models herein. The objective is to minimise wingbox mass, whilst attaining a specific lift distribution via passive elastic deformations and active deflections of the aerodynamic control surfaces.

The proposed design and optimisation strategy is shown to be able to produce a considerable change in the spanwise loading by shifting the wing centre of pressure inboard. An approximatively linear lift distribution, particularly suited for structural efficiency and stall recovery, is achieved. In addition, the optimisation produces aerostructural designs dominated by torsional loads, therefore leading to higher bend-twist coupling and more stringent shear strength requirements.

The remainder of the paper is structured as follows: Section 2 describes the reference wing model adopted for this study. Section 3 presents the aeroelastic methodology

[1] Ph.D. Research Student.
[2] Royal Academy of Engineering Airbus Sir George White Professor of Aerospace Engineering, AFAIAA.
[3] Lecturer in Composite Structures, Advanced Composites Centre for Innovation & Science (ACCIS).
[4] Honorary Research Fellow

used to calculate aerodynamic loads and elastic deformations. Relevant models for composite laminates and composite design guidelines are introduced in section 4. The optimisation problem, its design variables, constraints and the objective function are described in section 5. Finally, results are discussed and conclusions are drawn in sections 6 and 7, respectively.

2. Baseline Aeroelastic Wing Model

The model is representative of a state-of-the-art regional commercial jet—more specifically, of a short-to-medium-range aircraft designed for transonic speeds.

The structural finite element (FE) model is a right cantilevered half-wing with conventional architecture, i.e. a wingbox with front and rear spars along the entire span. The wing skins have stiffeners regularly spaced in the chordwise direction, represented by the dashed lines on the left-hand-side of Figure 1. Ribs, spars and stiffeners are made of Aluminium 7050–T7651. The wing skins are made of symmetric and balanced composite laminates. Upper and lower wing skins are divided into five partitions. The wingbox has straight ribs, aligned with the free stream and distributed uniformly within each of the five partitions. The laminates' stacking sequence is comprised of blocked stacks of $[\pm 45°/0°/90°]_s$ for a normalised ply distribution as shown in Figure 2. These values are found allowing the maximum Tsai-Wu ply failure index for a 2.5g symmetrical pull-up manoeuvre to be 0.75 (1 meaning damage). Material properties are shown in Table 1.

Inertial effects due to leading and trailing edge sub-structures and fuel weight are approximated by means of lumped masses connected to the spars via interpolation rigid elements. An additional lumped mass is placed at the aircraft centre of gravity (CG) to represent fuselage, payload, empennage and reserve fuel.

The wingbox is modelled in NASTRAN with CQUAD4 elements for skins, spars and ribs and CBAR elements for stiffeners. NASTRAN's doublet lattice model is used for computing steady aerodynamic loads. Similarly to [18], 20 discrete trailing edge ailerons are distributed along the wingspan. These devices occupy approximately 15% of the local wing chord. Their contribution to the wing inertia is represented with lumped masses placed at the mid-position of the hinge line. The masses are assumed to be proportional to the flaps' area.

The aerodynamic panelling consists of 2820 boxes. The panels are distributed evenly spanwise and following a cosine mesh chordwise. The aerodynamic mesh for the control surfaces is finer (see Figure 1) in order to capture rapid changes of pressure due to flap deflections.

The interpolation between the structural and aerodynamic degrees of freedom is based on the finite plate 3D spline method as implemented in NASTRAN's SPLINE6 card.

Further details of the geometrical arrangement, thicknesses distributions and the aeroelastic FE model are shown in Figures 1 to 3.

Table 1: Composite and metallic material properties.

Composite material (Hexcel 8552 NMS 128/2)			
Property	Value	Property	Value
E_{11}	148 GPa	X_{1t}	2439 MPa
E_{22}	10.3 GPa	X_{2t}	66 MPa
ν_{12}	0.27	X_{1t}	2013 MPa
G_{12}	5.9 GPa	X_{2c}	381 MPa
G_{23}	5.9 GPa	S_{12}	78 MPa
G_{13}	5.9 GPa	$S_{Bonding}$	34.7 MPa
ρ	1577 kg/m³		
*Temperature condition: -54°C			
Aluminium material (7050-T651)			
Property	Value	Property	Value
E	71.7 GPa	σ_Y	490 MPa
ν	0.33	ρ	2830 kg/m³

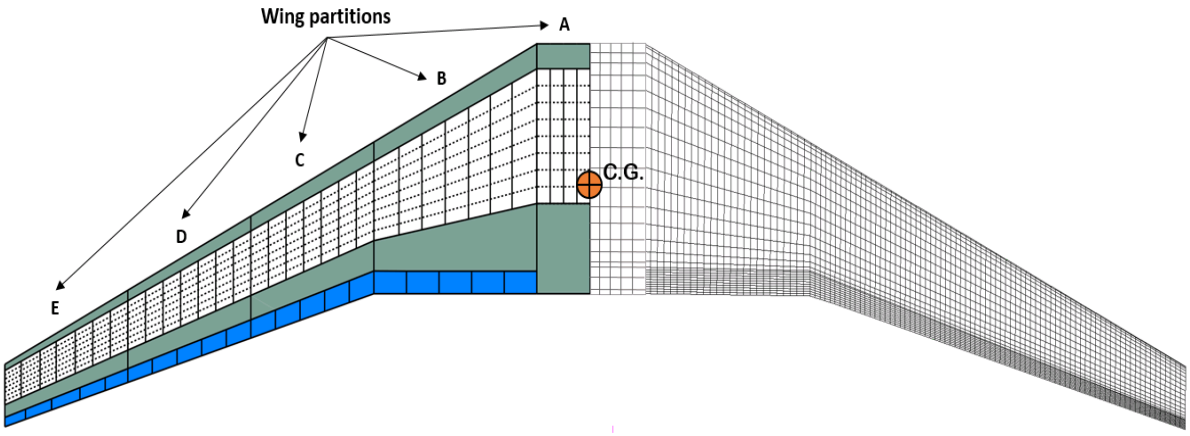

Figure 1: Details of the baseline wingbox arrangement and the aerodynamic panelling.

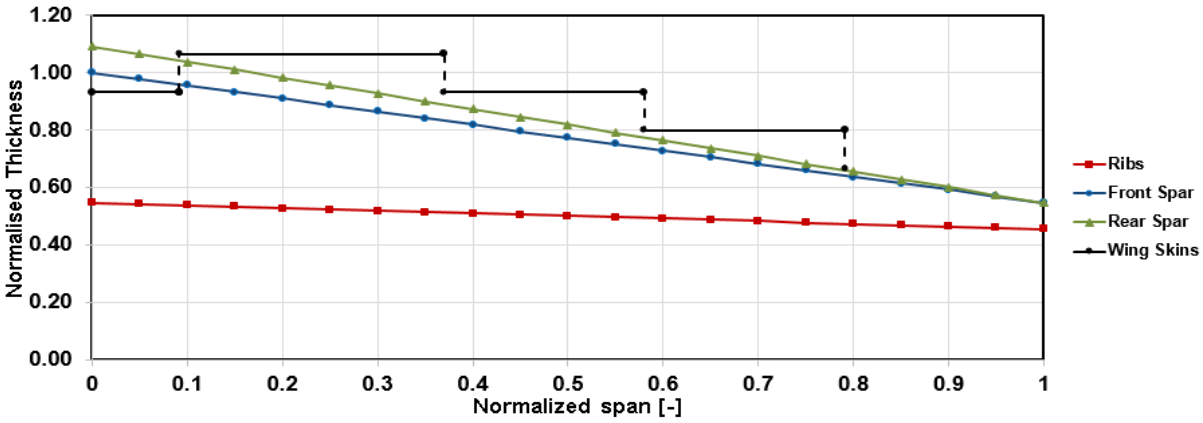

Figure 2: Thicknesses spanwise variations of the main wing structure components.

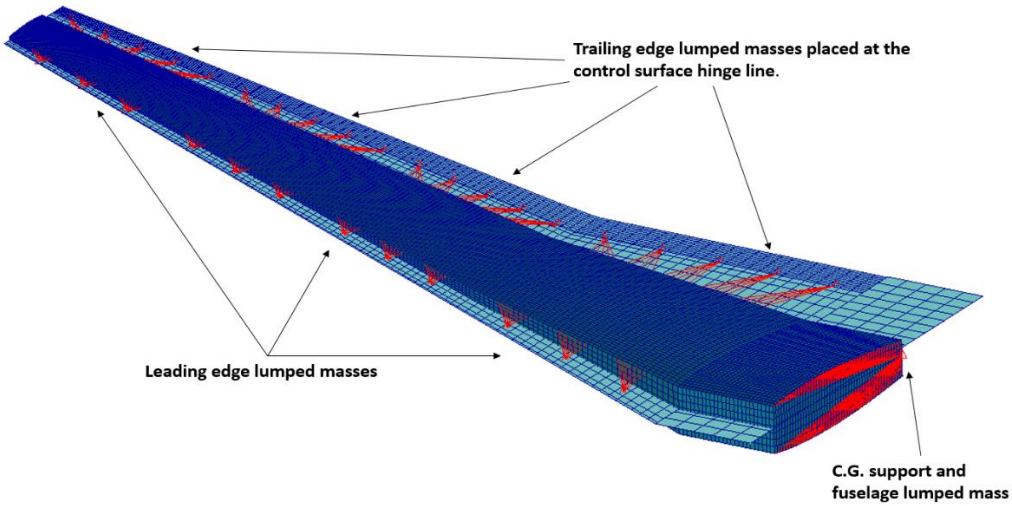

Figure 3: Structural FE model and aerodynamic mesh.

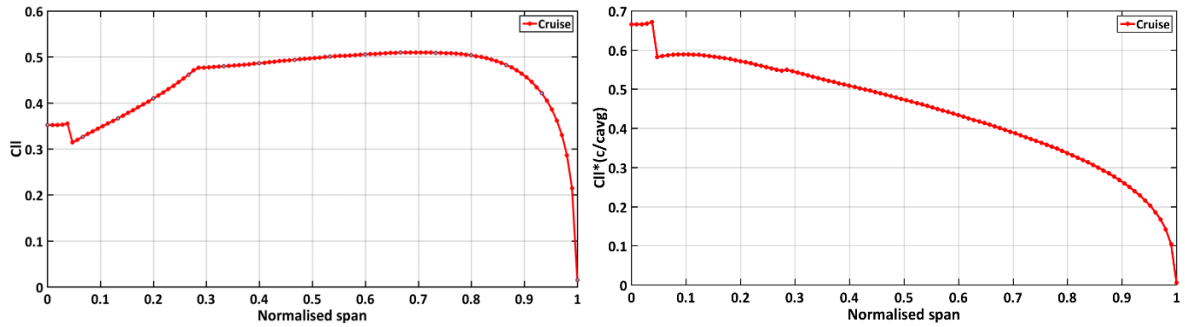

Figure 4: Spanwise loads at cruise condition.

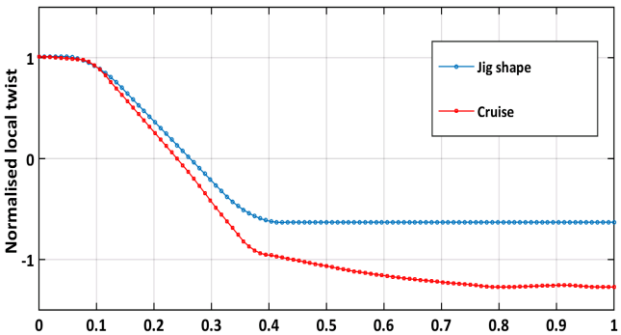

Figure 5: Local twist distribution of the Jig-Shape and cruise condition.

3. Static Aeroelasticity and Buckling Calculations

Two symmetric load cases are considered throughout this study: a 2.5g pull-up manoeuvre and a -1g manoeuvre, at Mach 0.82 and altitude h = 35000 ft. In both cases, full fuel mass is assumed (reserve fuel included. Note this is the value for the whole aircraft. Only one half is included in the FE semi-span model.).

Static aeroelastic loads and structural stresses are computed using NASTRAN solution 144. NASTRAN implements the Doublet-Lattice subsonic lifting surface theory (DLM) to calculate the aerodynamic loads. Since DLM uses a linear aerodynamic potential theory, effects of viscosity and aerofoil thickness are ignored. Structural nonlinearity and non-planar aerodynamic effects are also neglected. Consequently, constraints on maximum tip vertical displacement and maximum tip twist angle are applied to limit the structure to elastically linear deformations. The aerodynamic loads are transferred to the structural mesh via a finite surface spline (SPLINE6). Specifically, aerodynamic and structural degrees of freedom are interpolated using a surface spline connected to the FE nodes on the upper profile of spars and ribs.

A longitudinal trim analysis is performed to determine the loads acting over the wingbox. The trim variables used in this work are: angle of attack, pitch acceleration, normal load factor, pitch rate, and the deflections of the 20 control surfaces. Angle of attack and pitch acceleration are unknowns in the system of equations for trim equilibrium. The deflections of the control surfaces are fed to the system as know variables as found by the optimisation framework. The pitch rate is set to zero. Since the aircraft tail is not included in the analysis, an equivalent lumped mass is positioned at the CG of the aircraft to emulate airframe and payload inertial effects. This approach in turn causes a negligible, but non zero, pitching acceleration.

The spanwise lift loading is obtained from the local lift coefficient distribution, which, in turn, is calculated integrating the aerodynamic pressure coefficients chord-wise over the aerodynamic mesh.

Lastly, the aerodynamic loads are fed to NASTRAN solution 105 for a linear buckling analysis to examine structural stability. Five buckling eigenvalues and eigenmodes are computed and aggregated as a design constraint as explained in §5.1.2.

3.1 Static Aeroelastic Analysis of a Nominal Cruise Condition

Figure 4 shows sectional lift coefficient, C_{ll}, and span load coefficient, $C_{ll}c/c_{\text{avg}}$, for the baseline configuration flying at Mach 0.78 and altitude h = 33000 ft, with all control deflections set to zero. The rigid wing lift coefficient is C_L = 0.4778. When the flexibility of the structure is taken into account C_L = 0.4504.

From Figure 4 one can observe that, in the portion of the wing between 40% to 90% of the semispan, the load distribution is approximatively linear. Figure 5 shows the wing twist deformation at cruise, in comparison to the jig-shape. It is then inferred that the load distribution is due to geometric bend-twist coupling, because the baseline stacking sequence gives marginal material coupling and an overall negligible contribution to the aeroelastic deformation of the wing (this is shown in detail in §6.3).

4. Background Laminate Equations

For design purposes, wing structures are usually divided into many stiffened panels corresponding to individual, or clusters of, rib/stringer-bays. Consequently, an often impractical number of design variables is required to optimise the ply book (ply orientations in use and stacking sequence) for the whole airframe. This problem can be tackled using lamination parameters, an alternative way of modelling laminate stiffness that reduces the total number of design variables.

Typically, the in-plane stretching, [A], coupling, [B], and bending, [D], stiffness matrices that govern laminate behaviour can be found from classical laminate theory (CLT) [20,21], where they are functions of the stacking sequence and material properties.

According to CLT, elastic stresses induce a state of deformation described in terms of resultant forces, $N = \{N_x, N_y, N_{xy}\}^T$, and moments, $M = \{M_x, M_y, M_{xy}\}^T$, and related strains, $\varepsilon^0 = \{\varepsilon_x^0, \varepsilon_y^0, \gamma_{xy}^0\}^T$, and curvatures, $\kappa = \{\kappa_x, \kappa_y, \kappa_{xy}\}^T$ such that

$$\begin{bmatrix} N \\ M \end{bmatrix} = \begin{bmatrix} A & B \\ B & D \end{bmatrix} \begin{bmatrix} \varepsilon^0 \\ \kappa \end{bmatrix} \tag{1}$$

$$\begin{Bmatrix} N_x \\ N_y \\ N_{xy} \\ M_x \\ M_y \\ M_{xy} \end{Bmatrix} = \begin{bmatrix} A_{11} & A_{12} & A_{16} & B_{11} & B_{12} & B_{16} \\ & A_{22} & A_{26} & & B_{22} & B_{26} \\ \text{sym} & & A_{66} & \text{sym} & & B_{66} \\ B_{11} & B_{12} & B_{16} & D_{11} & D_{12} & D_{16} \\ & B_{22} & B_{26} & & D_{22} & D_{26} \\ \text{sym} & & B_{66} & \text{sym} & & D_{66} \end{bmatrix} \begin{Bmatrix} \varepsilon_x^0 \\ \varepsilon_y^0 \\ \gamma_{xy}^0 \\ \kappa_x \\ \kappa_y \\ \kappa_{xy} \end{Bmatrix} \tag{2}$$

For balanced, symmetrical and orthotropic laminates $A_{16} = A_{26} = 0$, and $B_{ij} = 0$.

Tsai *et al.* [20] and Tsai and Hahn [22] introduced an alternative representation for the stiffness characteristics of a laminate. This representation is based on twelve (eight when [B] = 0) lamination parameters, ξ_i^j, and five material invariants, U_k, with $i = 1, \ldots 4$, $j = A, B, D$, and $k = 1, \ldots 5$. The use of lamination parameters can be beneficial for optimisation purposes, because it reduces the number of design variables. In particular, [A] and [D] can be written as

$$\begin{bmatrix} A_{11} \\ A_{22} \\ A_{12} \\ A_{66} \\ A_{26} \\ A_{26} \end{bmatrix} = h \begin{bmatrix} 1 & \xi_1^A & \xi_3^A & 0 & 0 \\ 1 & -\xi_1^A & \xi_3^A & 0 & 0 \\ 0 & 0 & -\xi_3^A & 1 & 0 \\ 0 & 0 & -\xi_3^A & 0 & 1 \\ 0 & \xi_2^A/2 & \xi_4^A & 0 & 0 \\ 0 & \xi_2^A/2 & -\xi_4^A & 0 & 0 \end{bmatrix} \begin{bmatrix} U_1 \\ U_2 \\ U_3 \\ U_4 \\ U_5 \end{bmatrix} \tag{3}$$

$$\begin{bmatrix} D_{11} \\ D_{22} \\ D_{12} \\ D_{66} \\ D_{26} \\ D_{26} \end{bmatrix} = \frac{h^3}{12} \begin{bmatrix} 1 & \xi_1^D & \xi_3^D & 0 & 0 \\ 1 & -\xi_1^D & \xi_3^D & 0 & 0 \\ 0 & 0 & -\xi_3^D & 1 & 0 \\ 0 & 0 & -\xi_3^D & 0 & 1 \\ 0 & \xi_2^D/2 & \xi_4^D & 0 & 0 \\ 0 & \xi_2^D/2 & -\xi_4^D & 0 & 0 \end{bmatrix} \begin{bmatrix} U_1 \\ U_2 \\ U_3 \\ U_4 \\ U_5 \end{bmatrix} \tag{4}$$

where h is the laminate thickness and

$$\xi_{[1,2,3,4]}^A = \frac{1}{h} \int_{-h/2}^{h/2} [\cos 2\theta, \sin 2\theta, \cos 4\theta, \sin 4\theta] \mathrm{d}z \tag{5}$$

$$\xi_{[1,2,3,4]}^D = \frac{12}{h^3} \int_{-h/2}^{h/2} [\cos 2\theta, \sin 2\theta, \cos 4\theta, \sin 4\theta] z^3 \mathrm{d}z \tag{6}$$

with $\theta(z)$ corresponding to the ply angle along the through-thickness coordinate z.

To conclude, based on eqs. (5) and (6), $\xi_2^A = \xi_4^A = \xi_4^D = 0$ for balanced and symmetric laminates with ply orientations limited to ±45°, 0°, 90.

4.1 Laminate Design Guidelines

To ensure that the laminates output by the optimisation satisfy engineering and manufacturability standards, guidelines and design practice as per [23] are applied as design constraints. Specifically:

- Only four ply directions are allowed, i.e., ±45°, 0°, 90°.
- Laminates should be symmetric to eliminate membrane-bending coupling ($B_{ij} = 0$).
- A minimum of 10% of each ply direction must be present in the laminate.
- The laminate must be balanced ($A_{16} = A_{26} = 0$) to avoid extension-shear coupling, i.e. the number of -45° and +45° plies must be the same.
- At most four plies of the same thickness and orientation can be stacked together. This is to prevent matrix-cracking between layers.

5. Optimisation Problem Formulation

This paper investigates the trade-offs and synergies between passive and active aeroelastic adaptation for load alleviation and lightweighing. This is done by setting up two optimisations studies. In the first study, mass is minimised by only optimising the passive aeroelastic performance of the wingbox (the control surfaces are held at zero deflection). The second study includes active controls. The control surfaces are employed to reshape the lift distribution over the wing to reduce induced stresses. An aggregate objective function is used, where the first objective is minimum mass and the second objective is to minimise the distance between a target triangular-like spanwise loading and the spanwise loading of the j^{th} optimisation iteration at a fixed lift coefficient.

The aeroelastic problem is solved in terms of lamination parameters. The laminate ply-book is determined contextually, but within a separate optimisation. Recent work by [24-26] has demonstrated that this 'bi-level' approach provides an efficient way of solving the optimisation of laminated composite structures. Their design strategies typically combine gradient-based methods or integer linear programming, for the first level, and a permutation Genetic Algorithm (GA) or Particle-swarm Optimisation (PSO), for the second level.

We adopt a similar approach. The problem is broken down in an outer level gradient-based optimisation, where lamination parameters and thicknesses are used as design variables for mass minimisation, and an inner particle swarm optimisation level, where stacking sequences are found that meet manufacturing guidelines, whilst matching the lamination parameters obtained from the outer level. Constraints such as buckling, stress, strength and feasible regions for the lamination parameters [27] are applied at the outer level.

The optimisation scheme adopted here is represented in the flow chart of Figure 6. Starting with the baseline design of §2, aeroelastic sensitivities are calculated via finite differences by the gradient-based optimiser in the outer level (delimited by the solid black line). The design variables that define the stiffness properties of the composite skins are passed to the inner level optimisation (within the dashed line), where a particle-swarm algorithm is used to retrieve detailed stacking sequences.

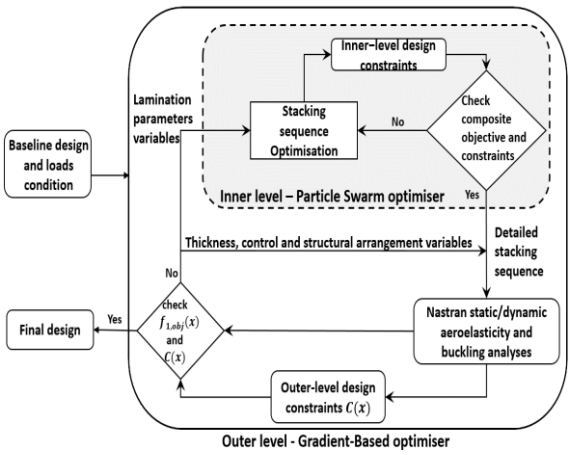

Figure 6: Bi-level optimisation framework combining Gradient-based and Particle-Swarm optimisations.

NASTRAN solution 144 is used to evaluate the performance metrics of the n^{th} set of design variables. MATLAB checks the constraints and computes the objective function. The process ends when one of the stopping criteria is met (i.e. thresholds for the optimisation step-size and first-order optimality measure).

5.1 Outer Level Optimisation Using Gradient-based Algorithm

Gradients of the objective function and gradients of the design constraints with respect to the design variables are estimated using MATLAB *fmincon* via central finite differences. Central finite differences have shown to be computationally more expensive, but more accurate in comparison to alternative methods. A standard interior-point algorithm is employed to solve the constrained optimisation problem.

5.1.1 Design Variables

The outer optimisation design variables consists of thicknesses of the metallic and composite panels (x_{t}), composite lamination parameters (x_{comp}), orientation and spacing of stringers and ribs (x_{sa}), and control surface deflections (x_{ctrl}). Each wing skin is divided into five patches, each with different thickness and lamination parameters. Spars and ribs thicknesses and the deflection pattern of the control surfaces, δ, are parameterized using an average sum of sine and cosine series. For a generic function f, discretised in $i = 1, \dots, n$ points, these series are defined as

$$f_i = \tfrac{1}{2}(f_{\cos}^i + f_{\sin}^i), \tag{7}$$

with

$$f_{[\cos,\sin]}^i = (1-\rho)\bar{f}_{[\cos,\sin]} + \rho\frac{(f_{\max}-f_{\min})}{(n-1)}i, \tag{8}$$

$$\bar{f}_{[\cos,\sin]} = f_{\min} + (f_{\max} - f_{\min})[\cos,\sin]\left(\frac{\pi}{i(n-1)}\right), \tag{9}$$

where ρ represents the clustering factor of the series, $f_{\max}$ and $f_{\min}$ denote the bounds to f. By changing the clustering factors, a wide range of curves can be achieved. To ensure that all variables are of the same order and avoid that the problem is indifferent to optimisation step-size variations, all unknowns are nondimensionalised and scaled to vary between 0 and 1.

Table 2: Type and number of the first level design variables.

Structural arrangement variables (x_{sa})		Control variables (x_{ctrl})	
Rib pitch	1	Max deflection	2
Rib orientation	1	Min deflection	2
Stringer pitch	1	Clustering factor 1	2
		Clustering factor 2	2
Total	3	Total	8
Composite variables (x_{comp})		Thickness variables (x_t)	
In-plane lamination parameter	20	Ribs	4
Out-of-plane lamination parameter	30	Front spar	4
		Rear Spar	4
		Wing skins	10
Total	50	Total	22
Maximum number of variables: 83			

Table 2 summarises the type and number of design variables used in this work. All thicknesses are bound between 2 mm and 16 mm. Control surfaces are allowed to move between –5 deg and 5 deg. Lamination parameters lie in the interval [-1,1], with additional restrictions discussed in §5.1.2. Rib orientation can vary from parallel to the free stream to perpendicular to the front spar.

5.1.2 Design Constraints

A number of constraints is applied in the optimisation routines to obtain realistic designs.

Structural stresses and buckling load factors are constrained using the Kreisselmeier–Steinhauser (KS) [28,29] aggregation method. The aggregation formula is given by

$$KS_{\text{metric}} = C_{\max} + \frac{1}{\rho_{KS}} \ln\left[\sum_{i=1}^{n} e^{\rho_{KS}(C_i - C_{\max})}\right], \tag{10}$$

where $C_{\max}$ is the maximum allowable constraint metric and C_i represents the value of the constraint metric for the i^{th} finite element/buckling load factor. The parameter ρ_{KS} represents the aggregation factor. Its value is set to 50 in order to avoid machine-zero errors. The advantage of the KS function lies in the fact that a large number of constraints can be combined into only one parameter.

Three different KS parameters are used to aggregate: (a) the Tsai-Wu composite failure index, where $C_{\max} = 1$, that is the maximum Tsai-Wu allowable value; (b) von–Mises stresses for the metallic sub-structures, where $C_{\max}$ equals the material maximum allowable stress, and (c) linear buckling load factors of different modes. KS values greater than one represents constraint violations.

Structural deformations such as tip twist angle and tip vertical displacement are also constrained. These constraints are expressed as

$$C_{\text{twist}} = \frac{\theta_{\text{tip}}}{\theta_{\text{allowed}}} \leq 1, \tag{11}$$

$$C_{\text{bending}} = \frac{z_{\text{tip}}}{z_{\text{allowed}}} \leq 1, \tag{12}$$

where θ_{allowed} is the maximum allowed tip twist angle and z_{allowed} denotes the maximum tip vertical displacement, which is limited to 20% of the semi-span. These limits ensure linear elastic behaviour.

As regards lamination parameters, one can retrieve feasible stacking sequences when the design space is bounded by the following equations [27]

$$\begin{gathered} 2\left(1+\xi_3^i\right)\left(\xi_2^i\right)^2 - 4\xi_1^i\xi_2^i\xi_4^i + \left(\xi_4^i\right)^2 \leq \left(\xi_3^i - 2\left(\xi_1^i\right)^2 + 1\right)\left(1-\xi_3^i\right), \\ \left(\xi_1^i\right)^2 + \left(\xi_2^i\right)^2 \leq 1, \\ 4\left(\xi_j^A + 1\right)\left(\xi_j^D + 1\right) - \left(\xi_j^A - 1\right)^4 \geq 0, \\ 4\left(\xi_j^A - 1\right)\left(\xi_j^D - 1\right) - \left(\xi_j^A - 1\right)^4 \geq 0, \\ -1 \leq \xi_j^i \leq 1, \end{gathered} \tag{13}$$

where $i = A, D$ and $j = 1, \dots, 4$. These inequalities are included in the optimisation as nonlinear constraints. They ensure convexity of the design space, a property that guaranties retrieval of global, rather than local, optima. Table 3 summarises the type and number of constraints used in the first level optimisation.

Finally, to guarantee that the aerodynamic loads are consistent, a redundant constraint is imposed on the total lift to make it equal to the aircraft weight. This is done to prevent sudden drops in aerodynamic loads that may arise due to poor aero-structural spline interpolations, which tend to occur because of architectural changes that can modify the spline configuration. This constraint is expressed as

$$C_{\text{lift}} = W \tag{14}$$

5.1.3 Objective Function

The objective function is the weighted sum of the aircraft wing weight and a lift spanwise loading parameter, SL. The loading parameter is expressed as a function of the square differences between a target spanwise loading and the calculated spanwise loading at the n^{th} gradient-based iteration:

$$f_{\text{obj1}}(x) = \alpha W + (1-\alpha) SL. \tag{15}$$

Here, W is the wing weight, α is a weighting factor and

$$SL = \sum_{i}^{N_L} \sum_{j}^{m} \left[\left(\frac{C_{ll}c}{c_{\text{avg}}}\right)_{i,j} - \left(\widetilde{\frac{C_{ll}c}{c_{\text{avg}}}}\right)_{i,j} \right]^2 \tag{16}$$

where, c_{avg} is the average chord length, $c(\eta)$ and $C_{ll}(\eta)$ are the local chord and lift coefficient. The parameter η is the normalized semi-span position, whilst i and j are indexes referring to load cases and the number of discretisation points along the semispan. Here, the target spanwise loading $\left(\widetilde{\frac{C_{ll}c}{c_{\text{avg}}}}\right)$ has triangular-like shape given by

$$P(\eta) = a\sqrt{1-\eta^2}(1 - \eta^2 + 0.25\eta^4), \tag{17}$$

where the coefficient a is calculated within the optimisation so to keep the integral of the lift distribution constant. In summary, the outer level optimisation problem can be stated as

$$\begin{gathered} \underset{x}{\text{minimise}}\, f_{\text{obj1}}(x) \\ \textit{with respect to: } x = \left\{x_{\text{t}}, x_{\text{comp}}, x_{\text{ctrl}}, x_{\text{sa}}\right\}^T \\ \textit{such that } C(x) = \begin{cases} KS^i_{\text{Mises}} \leq 1 \\ KS^i_{\text{Tsai-Wu}} \leq 1 \\ KS_{\text{Buckling}} \leq 1 \\ C^i_{\text{twist}} \leq 1 \\ C^i_{\text{bending}} \leq 1 \\ C^i_{\text{lift}} = W_{\text{MTOW}} \\ C\left(x_{\text{comp}}\right) \leq 0 \\ 0 \leq x \leq 1 \end{cases} \quad i = 1, \dots, N_L \end{gathered} \tag{18}$$

where $x = \{x_{\text{t}}, x_{\text{comp}}, x_{\text{ctrl}}, x_{\text{sa}}\}^T$ is the vector of design variables, $C(x)$ are the design constraints as a function of x and N_L is the number of static aeroelastic load cases.

Table 3: Type and number of constraints used in the first level optimisation problem.

Composite constraints		Structural constraints		Aeroelastic constraints	
Lamination parameters feasibility criteria	80	KS_{Mises}	2	C_{lift}	2
		$KS_{Tsai\text{-}Wu}$	2	C_{twist}	2
		$KS_{Buckling}$	1	$C_{bending}$	2
Total	80	Total	5	Total	6
Maximum number of constraints: 91					

5.2 Optimisation Scheme for Optimum Stacking Sequence (Inner level)

The goal of the inner level optimisation is to find a feasible stacking sequence that matches the in-plane and out-of-plane mechanical properties found in terms of lamination parameters in the first level optimisation.

For this optimisation problem, the design variables, $\bar{x}$, are the ply angles of each composite panel, constrained by the design guidelines of §4.1. The number of plies, and consequently the number variables is based upon the laminate thickness from the outer level.

The objective function is a weighted sum of square differences between the lamination parameters from the outer level, $\check{\xi}_j^{A,D}$, and the lamination parameters calculated at the n^{th} PSO iteration so that

$$f_{\text{obj2}}(\bar{x}) = \alpha \sum_{j=1}^{4} \left(\xi_j^A - \check{\xi}_j^A\right)^2 + (1-\alpha) \sum_{j=1}^{4} \left(\xi_j^D - \check{\xi}_j^D\right)^2 \qquad (19)$$

where the weighting factor α is set to 0.5.

6. Results Discussion

Results are presented for two different optimisation case studies: (i) a passive aeroelastic design, where the control surfaces are held at 0 deg, and (ii) a servo-aeroelastic wing, where a triangular spanwise distribution of load is set to be one of the objectives for the optimiser.

For reasons of brevity, results are presented for the most critical load case only, i.e. the 2.5g symmetric pull-up manoeuvre; Noting that all constraints and design objectives are meet for the -1g load case too.

6.1 Span Loads

First, we examine the spanwise lift distributions of the baseline and optimised designs. To simplify the results description, the case studies are labelled "OPT1" and "OPT2" to indicate the passive adaptive and servo-aeroelastic designs, respectively.

Figure 7(a) shows the spanwise variation of the sectional lift coefficient for all of the design cases. The baseline and OPT1 designs, have similar local lift distribution. This effect reveals a limited exploitation of the tailoring capabilities offered by composite materials. This is because the wing skin are divided into large partitions so, when active, the optimisation constraints influence the sizing of large portions of the structure, leading to a conservative design. Future developments will address this limitation by taking a more "local" tailoring approach, where the skins are optimised at rib/stringer-bay level.

The peak local lift coefficient occurs at approximately 75% of the semispan for the baseline and OPT1 designs. This indicates that the wing tip stalls first, producing an undesirable disruption in roll control and aileron effectiveness. For the OPT2 design, the peak C_{ll} is shifted considerably inboard, occurring at 27% of the semispan, showing improvements not only in the stall behaviour but also in structural efficiency (the wing root carries more load than the wing tip, therefore producing a smaller root bending moment).

The dimensionless span loads, $C_{ll}c/c_{\text{avg}}$, in Figure 7(b) shows that both initial and OPT1 designs have an approximatively triangular load distribution past the 40% of the semispan. This distribution results from a change in geometrical stiffness due to reductions in cross-sectional area. The span load distribution for OPT2 is clearly more triangular, with greater loads inboard. Intuitively, this loading shape is preferable from a structural standpoint, because the centre of pressure is shifted towards the inner wing, therefore reducing the root bending moment. Nevertheless, the load distribution in OPT2 does not match the target shape exactly. Analysing Figure 8(a), where a negative sign represents a downward surface deflection, and comparing the deflection pattern with the span loads in Figure 7(b), one can note that the optimised lift distribution is limited by the control deflections at the wing root. This limitation is associated with the parameterisation chosen for the control deflection scheduling. If the controls surfaces were allowed to move independently from each other, further improvements could be achieved. Similarly, a different target shape, where greater negative tip control deflections create negative lift (thus decreasing the bending moment even more), could lead to further weight reductions.

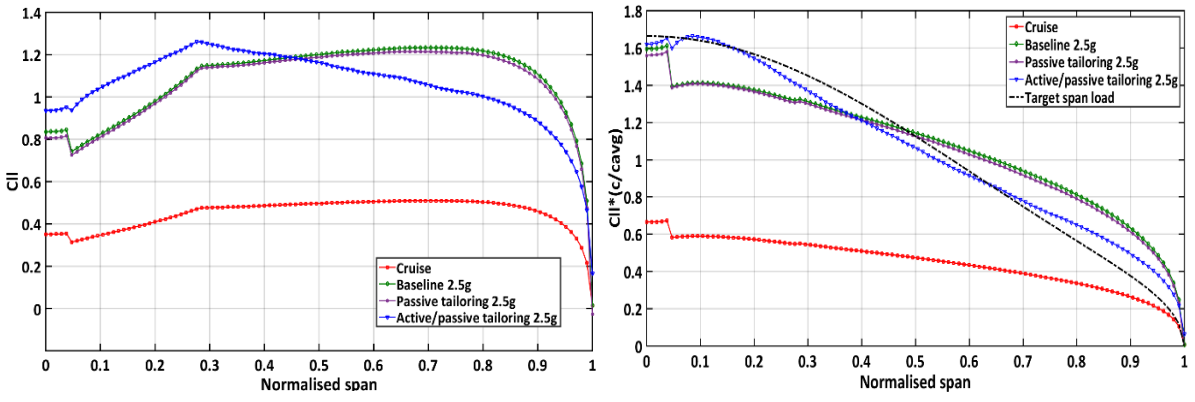

a) Sectional lift coefficient (C_{ll}) **b) Span loads $(C_{ll}c/c_{avg})$**

Figure 7: Aerodynamic loads comparison between different design studies.

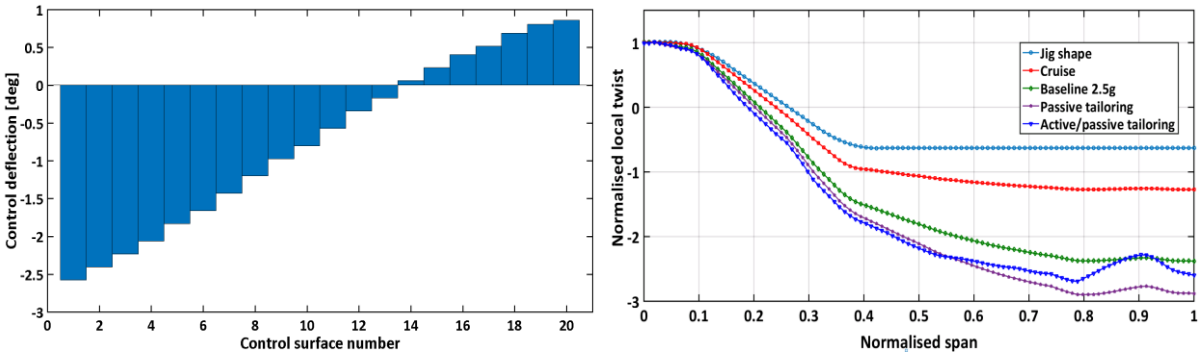

a) Control deflection scheduling for combined active and passive aeroelastic tailoring (2.5g load case)

b) Normalised local twist

Figure 8: Local elastic twist of different design studies and control surface deflections for the combined active/passive aeroelastic tailoring optimisation.

The plot for local twist deflections in Figure 8(b) shows the changes of torsional stiffness resulting from the optimisations. Both OPT1 and OPT2 have a considerable more pronounced elastic washout that the baseline. The increase in washout is due to changes of wing skins torsional stiffness and ribs orientation. All ribs, for both OPT1 and OPT2, are indeed set by optimiser to be perpendicular to the front spar, demonstrating that the gradient-based algorithm effectively finds the best configuration for minimum weight and passive load alleviation.

Outboard, OPT2, although lighter and more flexible, twists less than OPT1. The difference is more evident after 60% of the semispan, where the control surfaces transition from positive to negative deflections. This result demonstrates the synergy between passive and active wing adaptation, with the control surfaces redistributing the aerodynamic load to make it less demanding from a structural standpoint.

6.2 Optimum Wing Weight

In this section, we examine the weight build-up for OPT1 and OPT2. The wing mass (including leading edge and trailing edge lumped masses) and the updated MTOW are shown, respectively, in the first and second columns of Table 4. The percentage change in MTOW with respect to the baseline is also shown in the second column.

The wing weight for OPT1 and OPT2 is 12.41% of the MTOW and 11.63% MTOW, respectively, marking an improvement with respect to the baseline (13.51% MTOW).

For fixed MTOW, equal to the baseline, the change in wing weight allows the aircraft to carry an additional 1.25% and 2.13% of the baseline MTOW, respectively for OPT1 and OPT2 that can be converted into extra payload or additional fuel (i.e. greater range). The weight saving achieved translates into 7% additional passengers for OPT1 and 12% additional passengers for OPT2 (according to the average adult passenger with carry-on bags as defined by FAA regulations [30]). Note that this estimate does not include any extra weight necessary for prolonging the fuselage or accommodating extra seats.

Another possible way of using the weight gained with the optimisation is extending the aircraft range carrying additional fuel. Additional fuel would require additional tanks, thus increasing the operational empty weight (OEW) and reducing the net gain in terms of range or payload capacity. In this work, these effects are ignored.

Ref. [31] suggests using the payload-range efficiency parameter (PRE) to characterise and compare the performance of commercial aircrafts. This factor can be seen as the work done by unit of fuel consumed and is defined as

$$\text{PRE} = \text{payload} \times \text{range} \,/\, \text{fuel burnt}. \qquad (20)$$

Using Breguet's equation, the range, R, can be estimated from an aircraft's initial and final weight in a nominal cruise flight:

$$\text{R} = \frac{\text{V(L/D)}}{\text{SFC}} \ln\left(\frac{W_1}{W_2}\right) = \text{X} \ln\left(W_1/W_2\right) \qquad (21)$$

where W_1 is the initial weight, assumed to be 98% of the MTOW, W_2 is the final weight given by the sum of OEW and 4.5% of the MTOW in the form of non-consumed fuel, and X is the range parameter, which is related to the lift-to-drag ratio (L/D), the aircraft velocity (V) and the fuel specific consumption (SFC).

Table 4: Wing mass and payload gain for optimisation studies.

	Wing weight (full wing)	MTOW	Gain in payload or range		
Design	(% MTOW)	(% baseline change)	Passengers (% baseline change)	Range (% baseline change)	PRE/X for increased range (% baseline change)
Baseline	13.51%	(-)	(-)	(-)	0.2386
Passive tailoring (OPT1)	12.41%	-1.25%	+7%	+8.41%	0.2424 (+1.60%)
Active/Passive tailoring (OPT2)	11.63%	-2.13%	+12%	+14.39%	0.2450 (+2.67%)

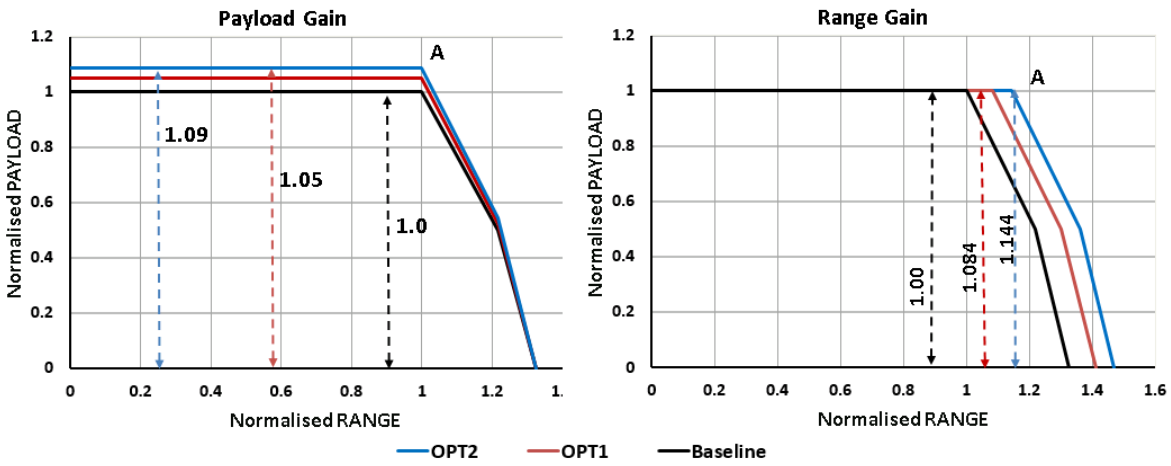

Figure 9: Thickness variations for optimisation study with combined active and passive aeroelastic tailoring.

A normalised net cruise range of '1.0' is assumed for the baseline design. Given this range and using the trends presented in [31], X can estimated is assumed constant and used for OPT1 and OPT2. The estimated improvements in range are show in Table 4 and in the simplified payload-range chart in Figure 9. Note that OPT1 and OPT2 can extend their range (point A) by approximately +8.41% and +14.39%, respectively.

6.3 Optimum Thickness distributions

Figure 10 and 11 show the ribs, spars and skins thicknesses for OPT1 and OPT2. In both cases, the lower skin is thicker than the upper skin, especially for the three inboard partitions. This result agrees with [32] and can be explained considering the combined effect of variations of section second moment of area, buckling and strength criter ia for the 2.5g load case. The overall change in skin thickness compared to the baseline (in Figure 2) is considerable for both design cases.

The normalised thickness of the ribs, as output by the optimisation algorithm, is constant all along the semispan and equal to 0.35 for OPT1 and 0.30 for OPT2.

The normalised thickness profiles for the front and rear spar in OPT1 are similar in magnitude and approximatively piecewise linear, changing from 0.81 at root to ~0.59 at the tip. In comparison to the baseline, one can note a considerable reduction of thickness at the root, of approximately 0.21 for the front spar and 0.28 for rear spar. Conversely, the normalised thickness of the wing tip changes by only 3%. The thickness in both spars plateaus on a constant value on the outermost 20% of the semispan.

Figure 11 shows an interesting thickness pattern for the spars of OPT2. Past 40% of the semispan, the rear spar carries more load than the front spar and is consequently substantially thicker. Both spars have minimum thickness at 85% of the semispan, followed by an increase towards the wing tip. This increment is consistent with the elastic twist and control scheduling in Figure 8 and is due to the fact that the wing tip carries less load as a result of the passive and active adaptation.

6.4 Wing Skin Stacking Sequence and Stresses

Tables 5 through 9 show the stacking sequences for the wing skins of OPT1 and OPT2 in terms of lamination (percentage of plies for each orientation), number of plies and a bend-twist coupling coefficient, $\bar{D}$. For comparison purposes, the stacking sequence of the baseline configuration is also shown. The bend-twist coupling coefficient is calculated using Equation (2) and is defined as

$$\bar{D} = \frac{D_{16}}{\left(D_{11}D_{22}^{3}\right)^{1/4} + D_{12} + 2D_{66}}. \text{ [23]} \qquad (22)$$

Some distinct characteristics emerge from the data. OPT1 and OPT2 are more flexible than the baseline and feature larger tip displacements. They are also lighter and therefore require a higher percentage of plies in the 0 deg direction to meet strength requirements (see table 5). Consequently, table 6 and 7 show that in relative terms OPT1 and OPT2 have less fibres than the baseline in the ±45 and 90 directions. Given the small number of partitions it is difficult to see clear distributions of stiffness, but some distinctive patterns seem to emerge indicating that the spanwise distribution of ±45 and 90 deg plies is related to torsional rigidity, structural integrity/stability, and to strength and manufacturing constraints.

Table 9 shows that the baseline behaves as a quasi-isotropic laminate, featuring small values for the bend-twist coupling coefficient. OPT1 and OPT2 exhibit different distributions of torsional stiffness. Nonetheless, both designs feature considerably larger bend-twist coupling coefficients than the baseline. This result has to be expected in wingboxes that are effectively designed to twist nose-down while bending for load alleviation.

Further insight and better design solutions could be gained by optimising smaller skin patches, as tailoring large partitions artificially restricts the design space available and can therefore lead to overly conservative and overly constrained solutions.

To visualise and compare the stress fields over the wing skins of OPT1 and OPT2, a plot of normalised von Mises stresses averaged through the laminate thickness is shown in Figure 12. Upper skins are thinner and locally carry higher stresses than lower skins. High stresses are located at the root and the mid-span partition, with peak values occurring at the leading and trailing edge and in the root and kink break areas. Considerable stress discontinuities can be seen as a result of the subdivision in large partitions. This result, once again, suggests that, for smoother stress fields and improved structural efficiency, tailoring should be done with blending constraints and at stringer/rib-bay level.

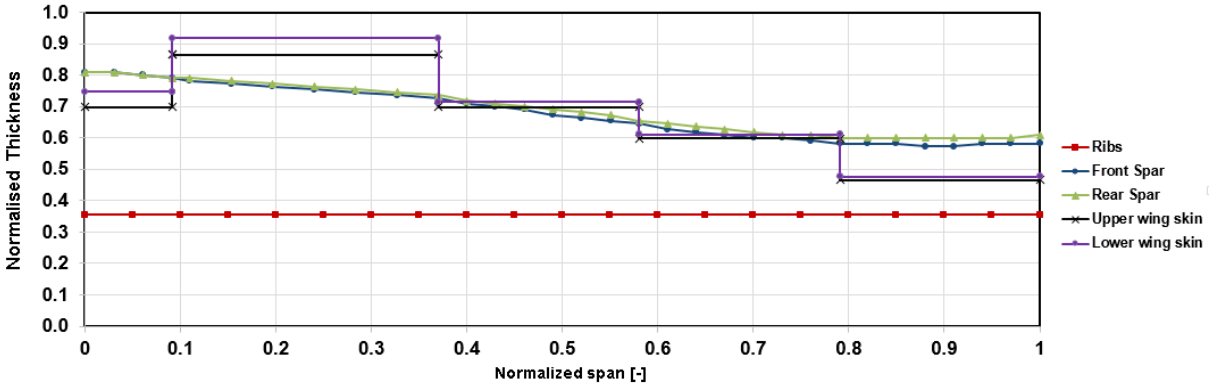

Figure 10: Thickness variations for the optimisation study with only passive aeroelastic tailoring.

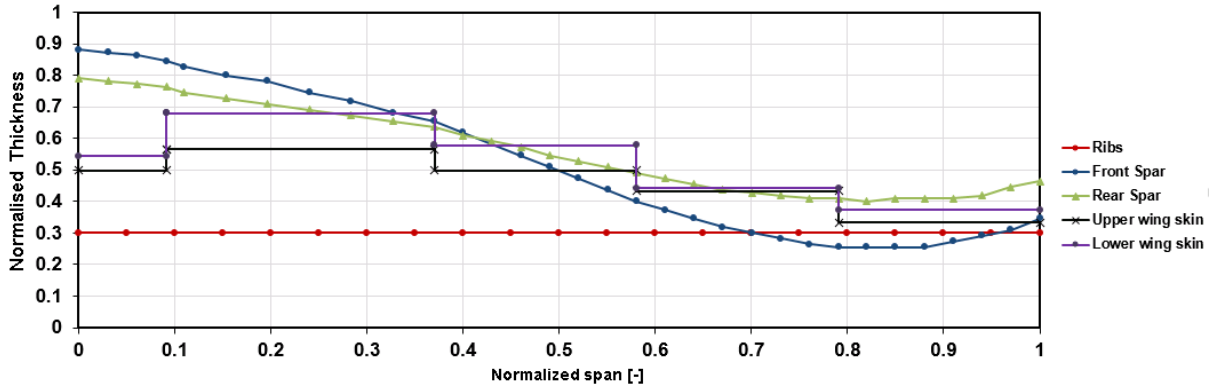

Figure 11: Thickness variations for optimisation study with combined active and passive aeroelastic tailoring.

Table 5: 0° ply fraction ($n_{0°}$)

Wing skin	Partition	Ply fraction ($n_{0°}$)		
		Baseline	OPT1	OPT2
Upper	A	0.25	0.2857	0.3333
	B	0.25	0.2692	0.4118
	C	0.25	0.2381	0.3333
	D	0.25	0.2778	0.3077
	E	0.25	0.2857	0.3000
Lower	A	0.25	0.2273	0.3750
	B	0.25	0.2222	0.3000
	C	0.25	0.2381	0.2353
	D	0.25	0.2778	0.3077
	E	0.25	0.2857	0.3636

Table 6: ±45° ply fraction.

Wing skin	Partition	Ply fraction ($n_{\pm 45°}$)		
		Baseline	OPT1	OPT2
Upper	A	0.50	0.4762	0.4000
	B	0.50	0.4615	0.4706
	C	0.50	0.4762	0.4000
	D	0.50	0.4444	0.4615
	E	0.50	0.4286	0.4000
Lower	A	0.50	0.4545	0.3750
	B	0.50	0.5185	0.4000
	C	0.50	0.4762	0.5882
	D	0.50	0.4444	0.4615
	E	0.50	0.4286	0.3636

Table 7: 90° ply fraction.

Wing skin	Partition	Ply fraction ($n_{90°}$)		
		Baseline	OPT1	OPT2
Upper	A	0.25	0.2381	0.2667
	B	0.25	0.2692	0.1176
	C	0.25	0.2857	0.2667
	D	0.25	0.2778	0.2308
	E	0.25	0.2857	0.3000
Lower	A	0.25	0.3182	0.2500
	B	0.25	0.2573	0.3000
	C	0.25	0.2381	0.1765
	D	0.25	0.2778	0.2308
	E	0.25	0.2857	0.2727

Table 8: Number of plies.

Wing skin	Partition	Number of plies (half stack)		
		Baseline	OPT1	OPT2
Upper	A	28	21	15
	B	32	26	17
	C	28	21	15
	D	24	18	13
	E	20	14	10
Lower	A	28	22	16
	B	32	27	20
	C	28	21	17
	D	24	18	13
	E	20	14	11

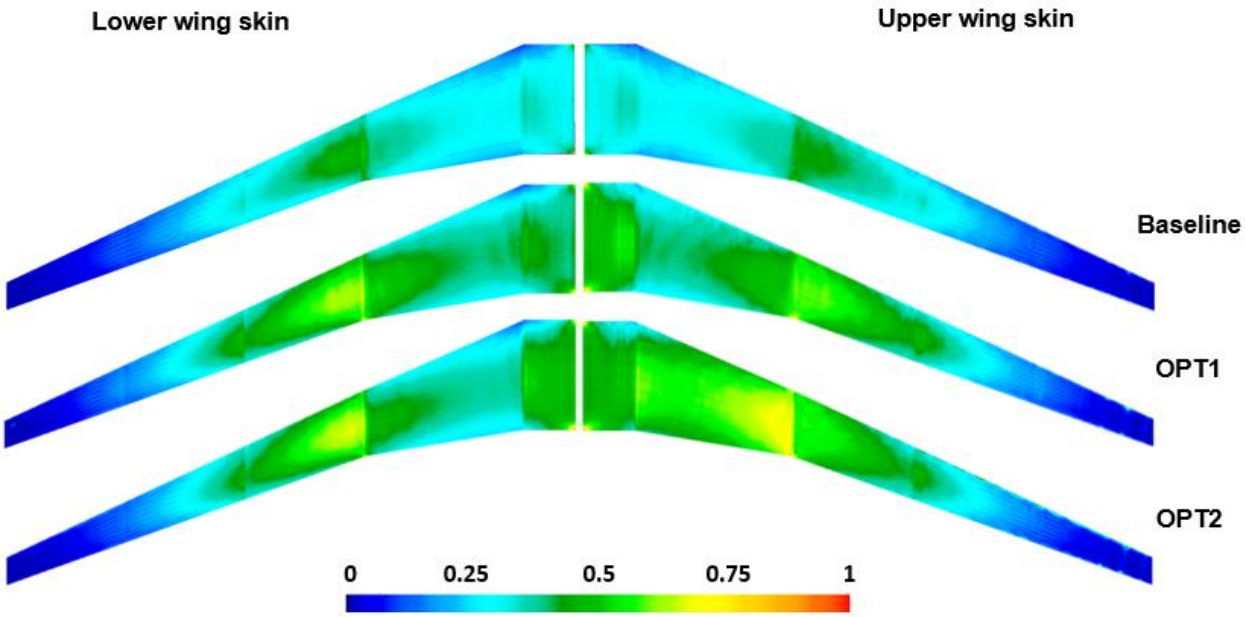

Figure 12: Normalised von Mises stress for the baseline and optimised design.

Table 9: Bend-twist coupling ratio.

Wing skin	Partition	Bend-twist coupling ratio (10^{-3})		
		Baseline	OPT1	OPT2
Upper	A	7.7	33.6	5.9
	B	6.7	53.1	39.3
	C	7.7	30.1	77.3
	D	9.0	29.8	12.3
	E	11.0	31.3	31.7
Lower	A	7.7	30.0	26.8
	B	6.7	32.8	49.0
	C	7.7	29.4	61.2
	D	9.0	17.4	9.8
	E	11.0	27.0	27.4

7. Conclusions

A servo-aeroelastic wingbox design is presented that exploits active and passive shape adaptation for improved aerostructural performance. Specifically, the wing, which is a metal/composite hybrid representative of a medium-range commercial airliner, is designed for minimum weight and, in turn, improved range and/or payload capacity. A bi-level optimisation framework, incorporating gradient-based and particle swarm algorithms, is used to tailor the wing components and retrieve optimal stacking sequences for the composite parts. The design objective is to minimise weight via optimal sizing and material arrangements that yield structural washout. Washout is sought as a means to modify the wing spanwise lift distribution for load alleviation.

Three designs are analysed: (i) a baseline, (ii) a wingbox with material and geometric bend-twist coupling and (iii) a servo-aeroelastic wingbox with bend-twist coupling and distributed aerodynamic control surfaces.

As expected, results show that the case study with the largest design space, i.e. the servo-aeroelastic design, produces greatest weight reductions. Distributed trailing edge devices allow the lift distribution to be shaped for improved load alleviation, producing an increase in payload/range of 12%/14.4%.

Both aeroelastic designs, are more flexible in bending and carry higher torsional loads in comparison to the baseline. Large wing skin partitions are tailored as a compromise between the accuracy required for a proof-of-concept type study and computational efficiency. This choice has produced sharp changes in thickness and nonuniform stress fields. These features suggest that results are conservative and could be further improved by tailoring the wing skins at stringer/rib-bay level and introducing composite patches blending constraints.

Acknowledgements

E.P. Krupa greatly acknowledges the support of the CNPQ, Conselho Nacional de Desenvolvimento Científico e Tecnológico – Brazil, under the scholarship 201386/2014-3 granted to pursue a PhD at the University of Bristol.

References

[1] Shirk, M., Hertz, T., Weisshaar, T., "Aeroelastic Tailoring – Theory, Practice, Promise," Journal of Aircraft, Vol. 23, No. 1, pp. 6-18, 1986.

[2] Kuzmina, S., Amiryants, G., Schwseiger, J., Cooper, J., Amprikidis, M., Sensburg, O., "Review and Outlook on Active and Passive Aeroelastic Design Concepts for Future Aircraft," ICAS 2002 Proceedings, International Council of the Aeronautical Sciences/AIAA, 2002.

[3] Stanford, B, K.; Wieseman, C, D.; Jutte, C, V., "Aeroelastic Tailoring of Transport Wings Including Transonic Flutter Constraints," AIAA SciTech Conference, 56th Structures, Structural Dynamics, and Materials Conference, Kissimmee, FL, 5 – 9 January, 2015, AIAA Paper 2015-1127.

[4] Jutte, C,V., Stanford, B, K.; Wieseman, C, D.; Moore, J, B., Aeroelastic Tailoring of the NASA Common Research Model via Novel Material and Structural Configurations. AIAA SciTech Conference, National Harbor, MD, January 13-17, 2014. AIAA Paper 2014-0598.

[5] Stanford, Bret K.; Jutte, Christine V., "Trim and structural Optimisation of Subsonic Transport Wings using Nonconventional Aeroelastic Tailoring," AIAA Scitech Conference, 56th Structures, Structural Dynamics, and Materials Conference, Kissimmee, FL, 5 – 9 January, 2015, AIAA Paper 2015-2596.

[6] Stodiek, O., Cooper, J., Weaver, P., Kealy, P., "Improved Aeroelastic Tailoring Using Tow-Steered Composites," Composite Structures, Vol. 106, pp. 703-715, 2013.

[7] Stodiek, O., Cooper, J., Weaver, P., Kealy, P., "Optimisation of Tow-Steered Composite Wing Laminate for Aeroelastic Tailoring," 56th Structures, Structural Dynamics, and Materials Conference, AIAA SciTech Conference, National Harbor, MD, January 13-17, 2014. AIAA Paper 2014-0343.

[8] Francois, G., Cooper, J. E., Weaver, P. M., "Aeroelastic Tailoring using Rib/Spar Orientations: Experimental Investigation," AIAA SciTech Conference, 56th Structures, Structural Dynamics, and Materials Conference, Kissimmee, FL, 5 – 9 January, 2015, AIAA Paper 2015-1408.

[9] Duke, D., Weisshaar, T., "Induced Drag Reduction Using Aeroelastic Tailoring with Adaptive Control Surfaces," Journal of Aircraft, Vol. 43, No. 1, Jan-Feb 2006.

[10] Ferrier, Y., Nguyen, N., Ting, E., "Real-Time Adaptive Least-Squares Drag Minimization for Performance Adaptive Aeroelastic Wing", 34th AIAA Applied Aerodynamics Conference, AIAA Aviation, Washington, D.C., 13-17 June, 2016.

[11] Burdette, D., Kenway, G., Martins, J., "Aerostructural Design Optmization of a continuous morphing trailing edge aircraft for improved mission performance" 17th AIAA/ISSMO Multidisciplinary Analysis and Optimisation Conference, AIAA Aviation, Washington, D.C., 13-17 June, 2016.

[12] Lin, J., "Active Aeroelastic Alteration to Reduce Off-Design Induced Drag", 17th AIAA/ISSMO Multidisciplinary Analysis and Optmization Conference, AIAA Aviation, Washington, D.C., 13-17 June, 2016.

[13] Nguyen, N., Lebofsky, S., Ting, E., Kaul, U., Chaparro, D., Urnes, J., "Development of Variable Camber Continuous Trailing Edge Flap Performance Adaptive Aeroelastic Wing," SAE Technical Paper 2015-01-2565, 2015.

[14] Ting, E., Dao, T., Nguyen, N., "Aerodynamic Load Analysis of a Variable Camber Continuous Trailing Edge Flap System on a Flexible Wing Aircraft," AIAA SciTech Conference, Kissimmee, FL, January 5-9, 2015.

[15] Nam, C., Kim, Y., "Optimal Design of Composite Lifting Surface for Flutter Suppression with Piezoelectric Actuators," AIAA Journal, Vol. 33, No. 10, pp. 1897-1904, 1995.

[16] Sahoo, D., Cesnik, C., "Roll Control of UCAV wing Using Anisotropic Piezoelectric Actuators", 43rd AIAA Structures, Structural Dynamics, and Material Conference, April 22-25, 2002.

[17] Stanford., B., "Optimisation of an Aeroservoelastic Wing with Distributed Multiple Control Surfaces", 33rd AIAA Applied Aerodynamics Conference, June 22-26, 2015.

[18] Stanford., B., "Static and Dynamic Aeroelastic Tailoring with Variable Camber Control", AIAA SciTech, 15th Dynamics Specialists Conference, January 4-8, 2016.

[19] Vassberg, J., DeHaan, M., Rivers, S., Wahls, R., "Development of a Common Research Model for Applied CFD Validation Studies," AIAA Applied Aerodynamics Conference, Honolulu, Hawaii, August 10-13, 2008.

[20] Tsai S. W, Halpin J. C, Pagano N, J., Composite materials workshop. Stanford, CT: Technomic Publishing Co., Inc.; 1968. p. 223–53.

[21] Jones, RM., "Mechanics of Composite Materials", New York: McGraw-Hill Publishing; 1975.

[22] Tsai SW, Hahn HT. "Introduction to composite materials". Stamford, CT: Technomic Publishing Co., Inc.; 1980. [750 Summer St.].

[23] Bailie, J. Ley, R., Pasricha A., "A summary and review of composite laminate design guidelines", technical report NASA,NAS1-19347. Northrop Grumman-Military Aircraft Systems Division; 1997.

[24] Liu D, Toropov VV, Querin OM, Barton DC (2011), Bilevel optimisation of blended composite wing panels. J Aircraft 48:107 – 118.

[25] Bloomfield M,W., Herencia J, E., Weaver P, M., (2009), Enhanced two-level optimisation of anisotropic laminated composite plates with strength and buckling constraints. Thin-Walled Struct 47:1161 – 1167.

[26] Liu D, Toropov VV, Querin OM, Barton DC (2015), Weight and mechanical performance optimisation of blended composite wing panels using lamination parameters. Struct Multidisc Optim (2015) 52:549 – 562.

[27] Bloomfield MW, Diaconu CG, Weaver PM. On feasible regions of lamination parameters for lay-up optimisation of laminated composite structures. Proceedings of Royal Society 2009; A465 (2104):1123–43.

[28] Kreisselmeier, G., Steinhauser, R., "Systematic Control Design by Optimizing a Vector Performance Index", International Federation of Active Controls Symposium on Computer-Aided Design of Control Systems, Zurich, Switzerland, 1979.

[29] Liem, R, P., Kennedy, G, J., Kenway, G, K., Martins, Joaquim R. R. A., "Multimission Aircraft Fuel-Burn Minimization via Multipoint Aerostrucutral Optimisation", AIAA Journal, Vol. 53, No.1, January 2015.

[30] Advisory Circular, "Aircraft Weight and Balance Control", US. Department of Transportation, Federal Aviation Administration, FAA, AC No: 120-27E, June 2005.

[31] Nangia, R., K., "Efficiency parameters for modern commercial aircraft", The Aeronautical Journal, Vol 110, No 1110, August 2006.

[32] Kennedy, G, J., Kenway, G, K., Martins, Joaquim R. R. A., "High Aspect Ratio Wing Design: Optimal Aerostructural Tradeoffs for the Next Generation of Materials," 52nd Aerospace Sciences Meeting, AIAA SciTech Conference, National Harbor, MD, January 13-17, 2014. AIAA Paper 2014-0596.